Influence of groundwater composition on the reductive precipitation of U(VI) on corroding iron foil surfaces

Journal of Nuclear Materials 577 (2023) 154324

Contents lists available at ScienceDirect

Journal of Nuclear Materials

journal homepage: www.elsevier.com/locate/jnucmat

Influence of groundwater composition on the reductive precipitation of U(VI) on corroding iron foil surfaces

N.L. Hansson[a,*], M. Saleh[a], P.L. Tam[b], S. Holgersson[a], K. Spahiu[a,c], C. Ekberg[a]

[a] Nuclear Chemistry / Industrial Materials Recycling, Chalmers University of Technology, SE-412 96 Gothenburg, Sweden
[b] Department of Industrial and Materials Science, Chalmers University of Technology, SE-412 96 Gothenburg, Sweden
[c] Swedish Nuclear Fuel and Waste Management Co., SE-101 24 Stockholm, Sweden

ARTICLE INFO

Article history:
Received 12 July 2022
Revised 5 February 2023
Accepted 6 February 2023
Available online 8 February 2023

Keywords:
U(VI)
Fe(II)
XPS
Reduction
Precipitation
Groundwater

ABSTRACT

In order to assess the disposal of spent nuclear fuel in a deep geological nuclear waste repository, the interactions between U(VI) and corroded iron present in the canister material are of importance. It is important to correctly model the fate of the oxidatively dissolved uranium in order to correctly estimate radium releases from the canister in the long term. The release of radionuclides into the environment depends on the dissolution of the UO_2 matrix which is dependent on the redox conditions at the fuel surface. The effect of metallic iron on the reduction of U(VI) was studied under anoxic conditions using synthetic groundwaters with different compositions, chosen to investigate the influence of calcium-uranyl-carbonato complexes on the thermodynamics and kinetics of U(VI) reduction on anoxically corroding iron. The corrosion products formed on the iron surface were investigated using SEM-EDS and XPS to identify elemental composition and oxidation states of uranium and iron on the surface. The iron foils efficiently reduced U(VI) to U(IV) causing its significant sorption and precipitation on the iron foil surfaces in the form of U(IV).

1. Introduction

A deep geological repository is the primary design considered for high-level radioactive waste disposal in Sweden. At the geological repository depth (500 m), conditions will quickly become anoxic after repository closure [1–3]. Oxidizing conditions in a canister failure scenario are therefore dependent on the production of radiolytic oxidants due to the radiation field of the fuel. A canister breach followed by groundwater intrusion could consequently result in oxidizing conditions locally at the UO_2-H_2O interface, leading to oxidation of the close to stoichiometric UO_2 in spent fuel to the much more soluble U(VI) state. The high solubility of the U(VI) state could cause oxidative dissolution of the UO_2 fuel matrix, followed by release of highly radiotoxic nuclides [4].

The KBS-3 concept is developed by the Swedish Nuclear Fuel and Waste Management Co, (SKB) in collaboration with Posiva Oy, and the first example of a repository using this concept is currently under construction in Finland at the Olkiluoto reactor site. In this repository concept, the fuel assemblies are inserted in massive iron inserts which are housed inside the copper canister [5]. In contact with groundwater, the iron inserts corrode extensively under anoxic conditions, thereby forming mainly magnetite and significant amounts of Fe(II) and H_2 in the process [6]. Several studies have shown that both dissolved hydrogen and Fe(II) considerably suppress the fuel corrosion rate [7–9]. For this reason, in the safety assessment of the repositories, a low rate of oxidative fuel dissolution is usually assumed. Despite the low assumed oxidative dissolution rate under these conditions, U(VI) is assumed to be formed and released due to the formation of radiolytic oxidants. This means that dissolved U(VI) will migrate further together with other released radionuclides. It is well known that U(VI) is reduced to U(IV) and sorbed and/or precipitated on the surface of metallic iron, both from studies made on ZVI (Zero Valent Iron) barriers [10–13] and also from studies related to waste disposal [14,15]. For example, the initial concentration of 1 ppm U(VI) decreased 2–3 orders of magnitude in a simplified groundwater solution consisting of 10 mM NaCl and 2 mM $NaHCO_3$ in contact with pure iron foils [15]. Characterization of the corroded iron foil showed that carbonate green rust was formed as corrosion product and UO_2 crystals were identified by XRD on the surface of the iron foil [15]. In the presence of anoxically corroding iron metal, U(VI) species may interact with either Fe(II) ions in solution, with anoxic corrosion products of iron formed in situ, or with the metal surface itself. Thus, a system with Fe metal present should have a higher

* Corresponding author.
E-mail address: nikhans@chalmers.se (N.L. Hansson).

https://doi.org/10.1016/j.jnucmat.2023.154324

reducing capacity than systems with only Fe(II) ions in solution or with only anoxic corrosion product of iron. Studies related to uranium contaminated sites with a series of Fe(II) containing minerals such as magnetite [16–18] or green rusts [15,19] have shown that U(VI) is efficiently reduced to U(IV), thereby decreasing its solubility.

Other studies have shown that the reduction of uranyl ions by dissolved Fe(II) depends strongly on the uranyl speciation. The abiotic reduction of U(VI) by Fe(II)(aq) and surface-bound Fe(II) is a fast process for free uranyl ions and its hydrolysis products but is slower for the uranyl-carbonato complexes, which might be due to a slower electron transfer for the uranyl-carbonato species [20,21]. Uranyl forms fairly strong complexes with carbonate [22] and the $UO_2(CO_3)_3^{4-}$ and $UO_2(CO_3)_2^{2-}$ complexes dominated the speciation calculations of U(VI) in most carbonate containing groundwaters until relatively recently, when it was discovered [23–25] that the uranyl-carbonato species bind strongly to Ca to form calcium-uranyl-carbonato complexes [26]:

$$UO_2(CO3)_3^{4-} + Ca^{2+} \rightleftharpoons CaUO_2(CO_3)_3^{2-},\ \log k = 5.2\pm0.2$$

$$UO_2(CO3)_3^{4-} + 2Ca^{2+} \rightleftharpoons Ca_2UO_2(CO_3)_3,\ \log k = 9.0\pm0.4$$

It has been shown that kinetic restrictions inhibit homogeneous reduction of the calcium-uranyl-carbonato species $CaUO_2(CO_3)_3^{2-}$ and $Ca_2UO_2(CO_3)_3$) by Fe(II)(aq), while ferrihydrite surface-catalyzed reduction of all aqueous uranyl by Fe(II) proceeds to U(V), which is incorporated into the ferrihydrite [27]. Several studies on the microbial reduction of uranium report changes in the kinetics of reduction of uranium in the presence of calcium [28,29], which limits microbial reduction of U(VI), likely due to steric and thermodynamic factors. A decreased sorption of U(VI) in the presence of Ca is also reported [30,31], which also indicates relatively strong Ca complexes.

The present work focuses on the interaction between corroded metallic iron and dissolved U(VI) in different simulated groundwater compositions under anoxic conditions. The main aim of the study was to investigate if calcium-uranyl-carbonato complexes hinder the U(VI) reduction by metallic iron. A combination of solution analysis and surface analysis allowed for oxidation states as well as compositions of the precipitated phases to be studied and the reductive precipitative effect to be assessed. The experiments give further insight into the reducing effect of corroding iron towards dissolved U(VI). This is important especially for the Swedish repository concept, because the main contributor to dose in the long term is radium [5]. If the release uranium is reduced on iron and remains in the canister, more radium will be produced in the long term by decay while less radium would be released from the canister if uranium is not reduced back on iron. Another issue is the correct modeling of the potential criticality in the canister in the long term [32] with dissolved actinides deposited back on iron as our study shows, or released in the far field if calcium uranyl carbonate complexes make the reduction impossible.

2. Materials and methods

2.1. Mass spectrometry

The uranium, iron and calcium concentrations were determined with an ICP-MS (Inductively Coupled Plasma Mass Spectrometry) instrument (Thermo Scientific iCAP Q). The measurements were performed using kinetic energy discrimination (KED) to better be able to discriminate iron and calcium from polyatomic ion interferences [33]. Samples and external standards were diluted using 0.5 M HNO_3 (Suprapur, Merck) spiked with 10 ppb Th from a 10 ppm certified standard solution (CPAchem) as an internal standard. External standards were made with 10 ppm Ca, Fe and U solutions (CPAchem) in the 0 – 50 ppb concentration range.

2.2. Surface analysis

X-ray Photoelectron Spectroscopic (XPS) measurements were conducted using PHI 5000 VersaProbe III scanning XPS microprobe with monochromatic Al K-α X-rays of energy 1486.6 eV [34]. Calibration was performed using the energy positions of argon-ion (Ar^+) sputter-cleaned gold (Au), silver (Ag) and copper (Cu) at which the core level peaks of $Au4f_{7/2}$, $Ag3d_{5/2}$, and $Cu2p_{3/2}$ are located at 83.96±0.05, 368.21±0.05 and 932.63±0.05 eV respectively [35]. A survey scan with larger step size (1.0 eV) was performed to identify the existing elements, after which narrow scans with smaller energy step size (0.1 eV) was performed on the regions of interest. Using these parameters, the detection limit is approximately 1.0 at.%. In general, 95% of the measured signal stems from the topmost few atomic layers [36]. The spectra were shifted with respect to the adventitious carbon C1s signal at 284.8 eV for analyses. Small pieces of the iron foils were transported in a transfer vessel tailored to the XPS sample introduction chamber to ensure transportation and sample introduction without risk of air contamination.

The energies of the U(IV), U(V) and U(VI) oxidation states in the $U4f_{7/2}$ peak, the width of the components (FWHM) as well as the relative shift of the satellite positions from the main peaks are shown in Table 1. The charging correction procedure in the instrument was shown in a previous work by our group to cause a shift in the U(IV) peak position on the surface of a UO_2 pellet to an energy of 379.5 eV [37]. A similar shift due to the charge correction procedure was seen in the work of Van den Berge et al. [38]. $Fe2p_{3/2}$ peak deconvolution was performed using the components shown in Table 2. The satellites of the Fe(II) and Fe(III) components were approximated as ~715 and ~718 eV respectively [39–41].

Small pieces of the foil surfaces were analyzed using a Phenom Tabletop scanning electron microscope (SEM) at 15 kV mode, equipped with energy dispersive spectroscopy (EDS).

2.3. Chemicals and synthetic groundwater composition

Iron foils with ≥99.99% purity (Thermo Scientific), 0.1 mm thickness and ~1.56 cm^2 surface area weighing 0.125 g were used in the experiments. The iron foils were polished with a #1200 grit (FEPA-P) SiC sandpaper in an inert-gas glovebox atmosphere to remove any pre-oxidized layer prior to the experiments. A 10 ppm U(VI) stock solution was mixed with the synthetic groundwaters resulting in an initial concentration of 1 ppm U(VI). The synthetic groundwater solutions were prepared using ≥99.0% ACS reagent grade chemicals (Sigma-Aldrich, Merck) in ultrapure water with a resistivity of 18.2 MΩ·cm (MilliQ Advantage, Merck). Two representative synthetic groundwaters from the repository depth at Forsmark, labeled “01D” and “02A” respectively, were prepared with concentrations given in Table 3 [51]. Two simplified synthetic groundwaters labelled “10–2″ and “10–2-Ca” were also studied. These both have a NaCl concentration of ~10 mM, and a HCO_3^- concentration of 2 mM, with 0.526 mM $CaCO_3$ included only in the “10–2-Ca” solution to isolate the influence of Ca^{2+}. The compositions of the four groundwater models are shown in Table 3. The iron and manganese additions to the synthetic groundwaters (Table 3) were done in the glovebox directly prior to experiment in order to minimize oxidation of these species.

$FeCO_3$ used in the oxygen traps was synthesized in an autoclave through mixing $FeSO_4{\cdot}7H_2O$, ascorbic acid, and ammonium carbonate in a 1:1:3 molar ratio which was allowed to react in 50 mL ultrapure water solution for 1.5 h at 140 °C as described

Table 1
Energy positions of the different uranium oxidation states and their associated satellite shifts.

U oxidation state	$U4f_{7/2}$ energy position (eV) [42–44]	FWHM (eV) [44,45]	Satellite shift (eV) [38,42,44,45]
U(IV)	380.0 ± 0.2	1.8 ± 0.2	6.9 ± 0.5
U(V)	380.8 ± 0.2	1.8 ± 0.2	8.5 ± 0.5
U(VI)	382.0 ± 0.2	1.8 ± 0.2	3.9 ± 0.5, 9.8 ± 0.5

Table 2
Energy positions of different iron oxidation states.

Fe oxidation state	$Fe2p_{3/2}$ energy (eV) [39,46-49]	FWHM (eV) [41,47,49,50]
Fe^0	706.7 ± 0.5	2.0 ± 0.5
Fe(II)oct	709.0 ± 0.5	2.0 ± 0.5
Fe(III)oct	711.0 ± 0.5	2.0 ± 0.5
Fe(III)tet	713.0 ± 0.5	2.0 ± 0.5

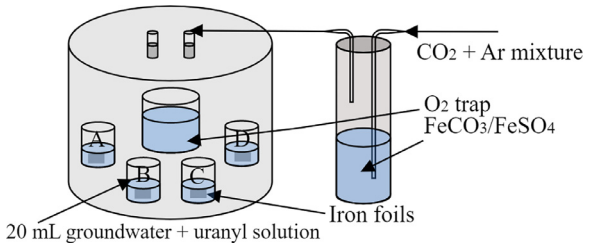

Fig. 1. Experimental setup for the iron foil experiments with reaction vessels (A, B, C, D) with groundwater + uranyl solutions and external gas washing bottle containing an O_2 trap. Also shown is the additional O_2 trap solution inside the reaction vessel. The setup is kept in the inert glove box atmosphere for the entirety of the experiment.

in the work of Nassar et al. [52], producing approximately 1 g of final product. $FeCO_3$ is significantly less soluble than $FeSO_4$, giving Fe(II) concentrations in the range of 10^{-4} M in close to neutral pH, also depending on the CO_2 pressure [53].

2.4. Experimental setup

The experiments were conducted in a glovebox with Ar atmosphere (Inert Technology). The glovebox atmosphere is continuously circulated past a catalytic bed that is removing O_2, maintaining a level of ≤0.1 ppm throughout the experiments. However, momentary air leaks through the antechambers or due to interruptions in Ar gas supply to the glovebox could briefly cause an increase in O_2 partial pressure. The glovebox was maintained at a room temperature of 20.0 ± 2.0 °C.

Solutions consisting of 2 mL 10 ppm U(VI) stock were diluted to 20 mL with the synthetic groundwaters in plastic vials which were placed in a ~2 L glass reaction vessel inside the glovebox. The reaction vessel was equipped with a gas inlet and outlet, which allowed for a continuous flushing of inert gas, making it possible to have a fixed atmosphere shared by all the experiments in a batch. The experimental setup can be seen in Fig. 1.

The batch experiments were labeled A-P (Table 4). For the batches A-D as well as I-L, the continuously flushing gas was also bubbled through a gas washing bottle containing 50 mL MQ with 2 g $FeSO_4$ and 2.5 g $CaCO_3$ to eliminate traces of O_2 in the gas mixture prior to flowing into the reaction vessel. For the experiment batches E-H and M-P, the gas was instead bubbled through a 50 mL solution saturated with $FeCO_3$ + 2.5 g $CaCO_3$. An additional 50 mL vial with a solution saturated with either $FeSO_4$ or $FeCO_3$ + 2.5 g $CaCO_3$, matching that of the gas washing bottle, were used as oxygen trap inside the reaction vessel. The gas used for flushing the batches consisted of 3000 ppm CO_2 in Ar for the batch containing the experiments A-D and 400 ppm CO_2 in Ar for the remaining batch experiments E-P. These were bubbled at a rate of ~3 bubbles per second through the gas washing bottle leading into the reaction vessel to ensure that a fresh atmosphere with known composition was maintained. Samples of ~0.1 mL were taken every ~48 h during the experiments, which lasted 750 – 1250 h.

Table 4
Groundwater and Atmosphere compositions and their corresponding experiment label.

Groundwater	Label
01D	A, E, I, M
02A	B, F, J, N
10–2	C, G, K, O
10–2-Ca	D, H, L, P
Atmosphere	Label
3000 ppm CO_2 in Ar	A, B, C, D
400 ppm CO_2 in Ar	E, F, G, H, I, J, K, L, M, N, O, P

3. Results

3.1. Concentration measurements

The measured data for dissolved Ca, Fe, and U concentrations in the experiment batches A-D under 3000 ppm CO_2 in Ar atmosphere and using the $FeSO_4$ O_2-trap are shown in Fig. 2. U concentrations start at 1 ppm ($4.2{\cdot}10^{-6}$ M), after which the concentrations gradually decrease to ~10^{-9} M towards the end of the 1200 h experiment for all four data series. Dissolved Fe is initially somewhat higher in A and B experiments, due to the Fe present in the 01D and 02A water compositions. Fe concentrations are then roughly equal for all the four series after ~200 h, after which the concentration reaches a value of almost 10^{-3} M in experiment A and B. In C and D, the concentrations are about two orders of magnitude lower, (~10^{-5} M). Ca concentrations were stable at initially set values for the whole experimental time period.

The measured data for dissolved Ca, Fe and U concentrations in experiment batch E-H under 400 ppm CO_2 in Ar atmosphere and using the $FeCO_3$ as O_2 trap are shown in Fig. 3. U concentrations decrease to 10^{-8}–10^{-7} M before increasing somewhat at the end of the experiment. The fluctuations that can be seen in Fig. 3 are

Table 3
Chemical compositions of the synthetic groundwaters. Concentrations in units mmol/L.

Ground-water	$[Na^+]$	$[K^+]$	$[Ca^{2+}]$	$[Mg^{2+}]$	$[HCO_3^-]$	$[Cl^-]$	$[SO_4^{2-}]$	$[Br^-]$	$[F^-]$	[Si]	$[Fe^{2+}]$	$[Mn^{2+}]$	$[Sr^{2+}]$	pH
01D	77.02	0.187	45.91	0.448	0.280	168.56	0.324	0.581	0.061	0.152	0.014	0.0016	0.237	8.40
02A	96.57	0.931	22.21	10.04	2.065	148.91	5.275	0.304	0.077	0.216	0.041	0.0377	0.099	7.19
10–2	12.00	0	0	0	2.000	10.00	0	0	0	0	0	0	0	8.34
10–2-Ca	10.47	0	0.526	0	2.000	9.00	0	0	0	0	0	0	0	8.34

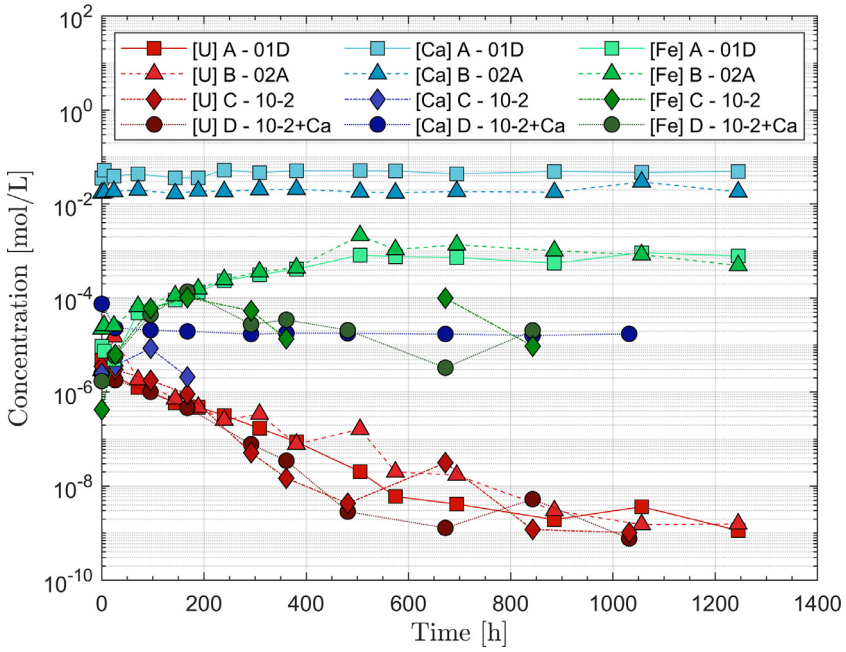

Fig. 2. Dissolved concentrations in the 3000 ppm CO_2 Ar atmosphere experiment batch A-D using the $FeSO_4$ O_2 trap.

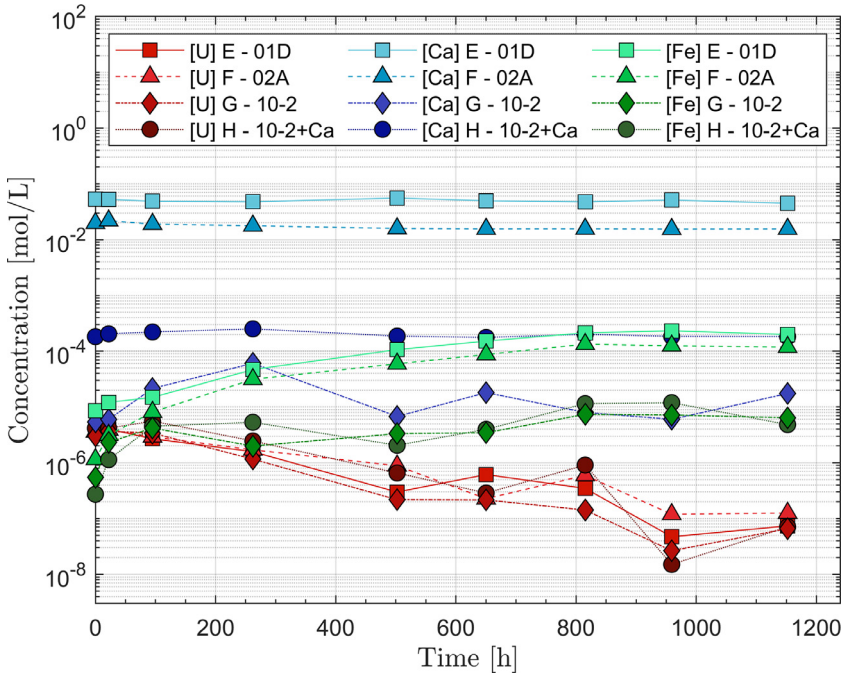

Fig. 3. Dissolved concentrations in the 400 ppm CO_2 Ar atmosphere experiment batch E-H using the $FeCO_3$ O_2 trap.

mainly believed to be due to influence of oxygen but might also possibly be due to colloid formation during the later stages of the experiment. Fe concentrations reach levels of 10^{-4} M in experiment series E & F, almost an order of magnitude lower than during the 3000 ppm CO_2 in Ar atmosphere series A & B (Fig. 2). Ca concentration levels are stable throughout the experiments. Interferences or a slight contamination leads to the Ca concentrations in experiment G, as there should be no Ca present in the 10–2 groundwater solution.

A duplicate series with batch experiments M-P, with identical experimental conditions as the one in the E-H experiments, was made. However, in the M-P series an O_2 contamination in the order of 80 ppm was detected (caused by an empty gas supply) which significantly influenced the data. The data series can be seen in the Appendix.

Finally, the measured Ca, Fe and U data for experiment batch I-L under 400 ppm CO_2 in Ar atmosphere with the $FeSO_4$ oxygen trap are shown in Fig. 4. In this series of experiments, U concentrations reach significantly lower values ($\sim 10^{-9}$ – 10^{-8} M) than the E-H experiment series ($\sim 10^{-7}$ M, see Fig. 3) but not as low as the A-D experiment series ($\sim 10^{-9}$ M, see Fig. 2). It is important to note that the duration of the I-L experiments was also somewhat shorter of 770 h than the previous two series of experiments (A-D and E-H). The dissolved Fe concentrations in series I & J reached concentra-

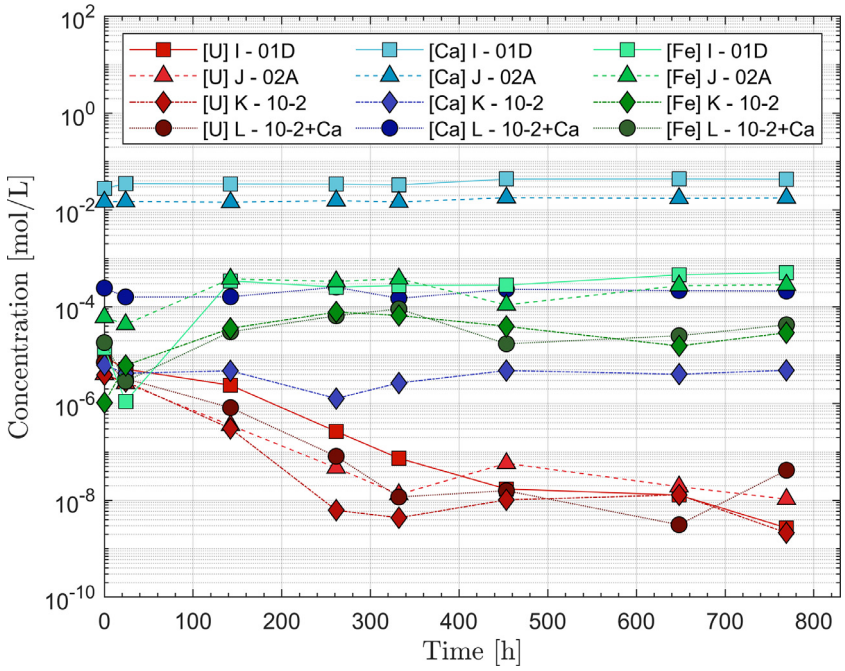

Fig. 4. Dissolved concentrations in the 400 ppm CO_2 Ar atmosphere experiment batch I-L, using the $FeSO_4$ O_2 trap.

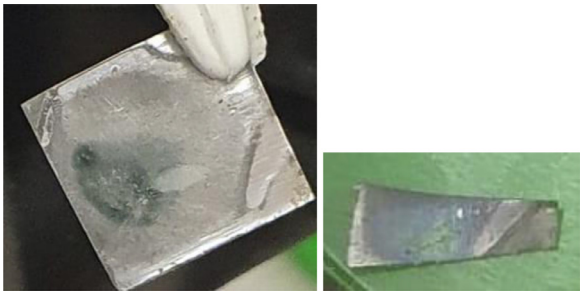

Fig. 5. a & b – Pictures of iron foil as well as a piece of iron foil, taken after leaching experiments E and F, respectively, where a clear green (a) and a green-bluish (b) rust spot is found.

tions of 10^{-4} M earlier than the corresponding experiments E & F. However, the higher levels of ~10^{-3} M Fe in the corresponding experiments A and B were never reached. Ca concentrations were stable in all experiments.

3.2. SEM/EDS

The iron foils showed dark-green spots after taken out of the synthetic groundwater solution (see Fig. 5a and Fig. 5b), a characteristic feature of green rust [54,55].

The SEM analysis was performed only on experiment batches E-H and I-L, due to oxygen contamination potentially impacting the other iron foil surfaces during sample storage (after the experiments). The SEM images of the iron foils from experiments E & F with groundwater simulants 01D and 02A are shown in Fig. 6a and b, respectively. The uranium is not distributed over much of the analyzed area but is rather agglomerated in a few grains like spots. According to EDS analysis, the iron foils from the experiments where the groundwaters 01D and 02A were used have several features with complicated compositions containing O, Na, Fe, Cl, C & Si. The precipitated uranium-containing grains on the foils have a much simpler composition based on the EDS analysis, presented in Table 5. The carbonate rich 02A water gave a higher carbon content in the uranium grains on the surface of iron foil F (8–16 at.%) as compared to 01D water that were used with iron foil E (1–5 at.%) based on ~5 analyzed grains per foil, however, the inclusion of oxygen in the compositional analysis considerably decreases the other elemental concentrations.

Table 5
EDS element compositions on iron foils E, F, G, H, K & L.

Element	E (at.%)	F (at.%)	G (at.%)	H (at.%)	K (at.%)	L (at.%)
O	57.15	–	–	63.06	47.58	60.72
Fe	24.61	54.22	24.26	12.42	10.61	13.40
U	15.12	34.33	60.78	19.50	32.71	19.90
C	3.13	11.45	14.96	5.02	9.09	5.98

An elemental mapping performed for a short duration on grains on the iron foil from experiment F showed that the uranium precipitates had a considerable overlap with carbon. The same was found on foils G & H, with carbon rich spots associated with the uranium precipitates. The SEM images of the iron foils from experiment G & H with groundwater simulants 10–2 and 10–2-Ca are shown in Fig. 7a and b respectively. The results are very similar to those from experiment E and F.

In experiment I using the 01D groundwater, uranium spots were detected in connection with ~4 at.% carbon content, which corresponds well with the results found in experiment E, where the same groundwater composition was used. Significantly larger uranium grains were found on the iron foil from experiment K compared to L, as shown in Fig. 8a and b respectively.

3.3. XPS

The XPS measurement is limited by the 100 µm X-ray beam size, which makes the characterization of individual uranium-containing deposits/uranium grains with a size smaller than 10 µm impossible. Nonetheless, the XPS analysis can give an overview about the surface chemistry of the iron foils after exposure to the uranyl-containing synthetic groundwaters. The core levels of $U4f_{7/2}$ and $Fe2p_{3/2}$ were analyzed. The U5f region at 0–2 eV as well as the valence band are clustered with energies from several of the ele-

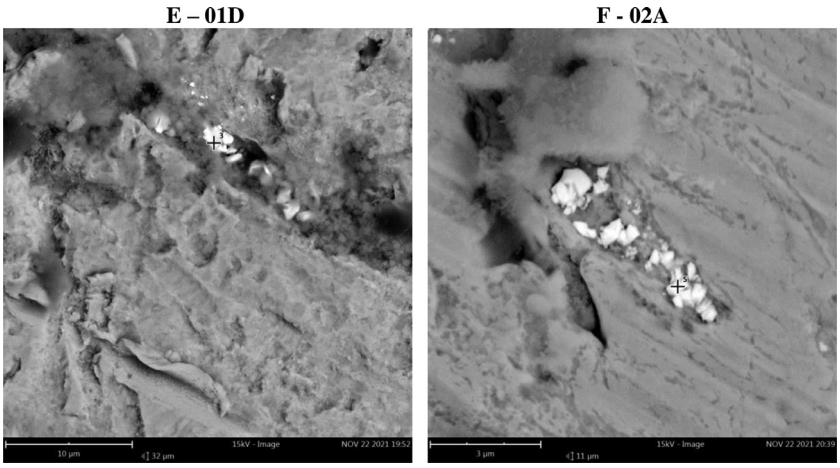

Fig. 6. a & b – SEM analysis on foils from experiments E (a) & F (b) showing rather large, precipitated uranium grains.

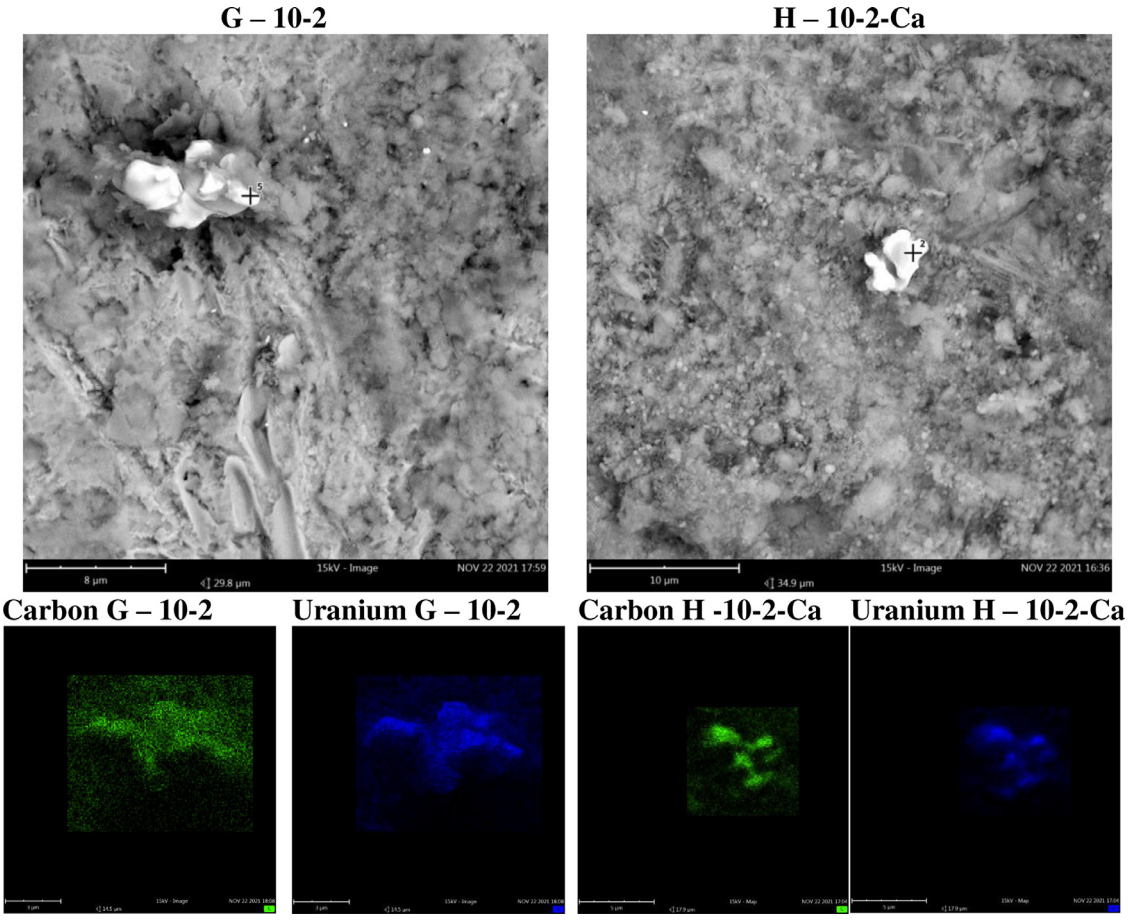

Fig. 7. a & b – SEM analysis and EDS mapping images on foils G (a) (leached with 10–2 water) & H (b) (leached with 10–2-Ca water). The significant overlap between carbon and uranium on the surfaces is shown from the brief elemental mapping scans.

ments present in the groundwaters, making it very difficult to analyze these regions, which were therefore left out of the analysis. This measurement was not performed on foils from experiments A-D, as the impact of oxygen contamination is significant to the batch.

Rather low amounts of uranium present in the experiment led to low peak intensity and noisy data. The $U4f_{7/2}$ XPS spectra from iron foils in experiments E-H are shown in Fig. 9. The FWHM of the peaks are all close to 1.8 eV, corresponding to a single oxidation state [44,45].

The $U4f_{7/2}$ & $U4f_{5/2}$ regions from the XPS measurements of the iron foils from experiment batch I-L are shown in Fig. 10. The FWHM of the peaks are all close that of a single oxidation state. However, the $U4f_{7/2}$-peaks of the iron foils from experiments I & K are located at approximately 1 eV lower energy compared to the $U4f_{7/2}$-peaks of experiments J, K as well as E-H.

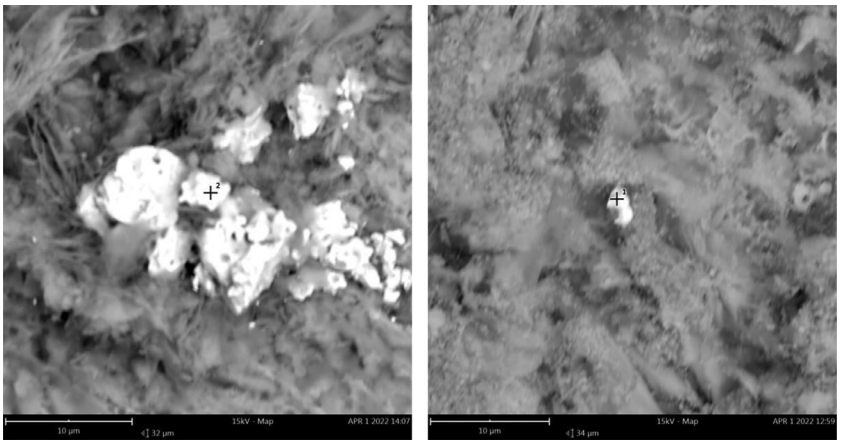

Fig. 8. a & b – SEM elemental analysis on foils K (a) (leached with 10–2 water) & L (b) (leached with 10–2-Ca water) showing the large, precipitated uranium-containing grains.

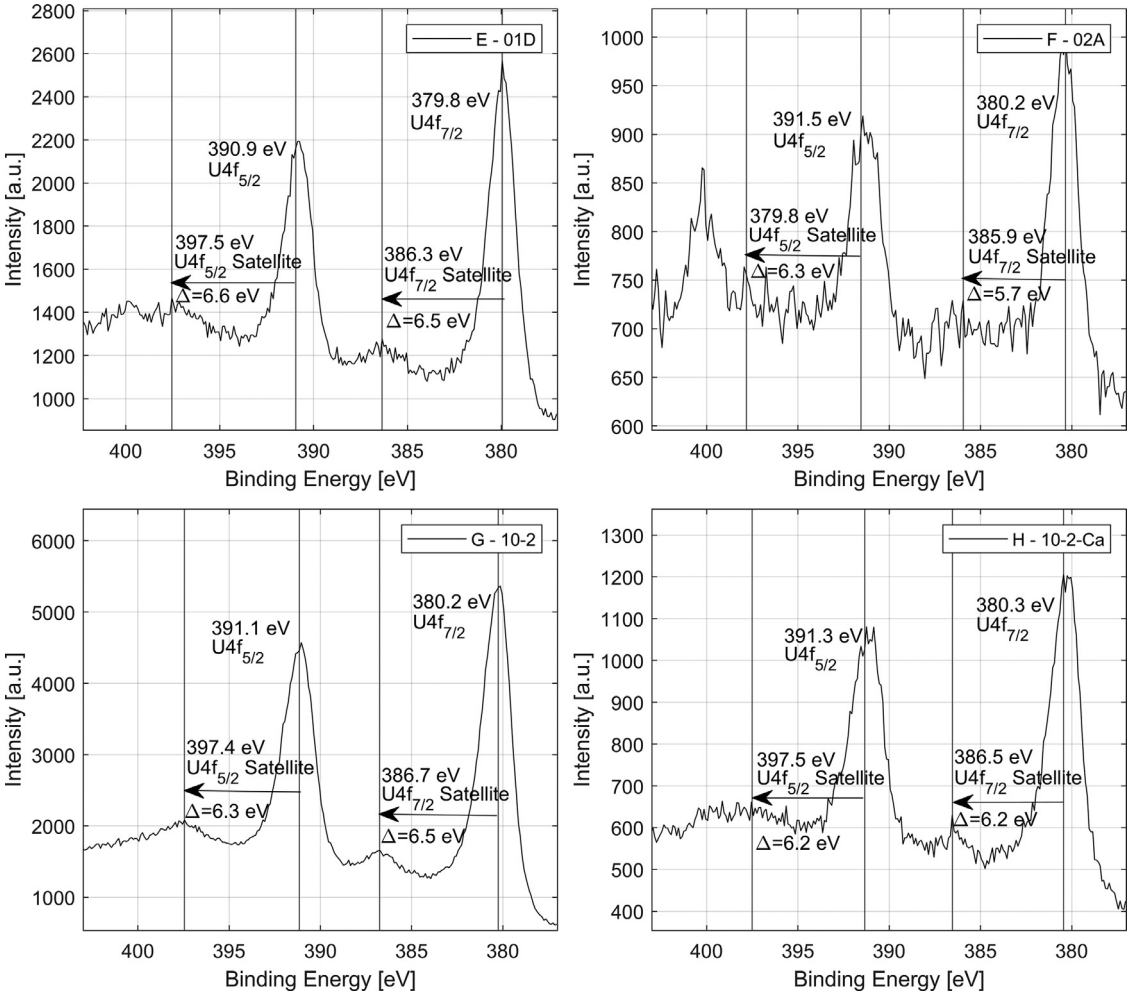

Fig. 9. XPS measurement of the $U4f_{7/2}$ & $U4f_{5/2}$ peaks with the corresponding satellites from experiment batch E-H.

A general spectrum on the iron foil from experiment M was found with a $U4f_{7/2}$-peak position of 380.3 eV, corresponding to a low oxidation state. Additionally, crystallite features that were not observed on the other iron foils, could be observed, which are likely due to the O_2 contamination during the experiment. The $U4f_{7/2}$ & $U4f_{5/2}$ regions of two crystallite features are shown in Fig. 11 with a higher oxidation state than what was observed in the general spectrum. The significantly higher $U4f_{7/2}$-peak energy on feature 2 indicate that certain spots were oxidized on the surface as U(VI), as the position is clearly above that of U(V). The oxidation therefore did not occur uniformly on the iron foil surface but was seemingly concentrated to spots which show stronger oxidation.

The $Fe2p_{3/2}$ peaks on the iron foils were analyzed and deconvoluted into their Fe(0), $Fe(II)_{oct}$, $Fe(III)_{oct}$, $Fe(III)_{tet}$, $Fe(II)_{sat}$ and $Fe(III)_{sat}$ signals corresponding to the characteristics shown in

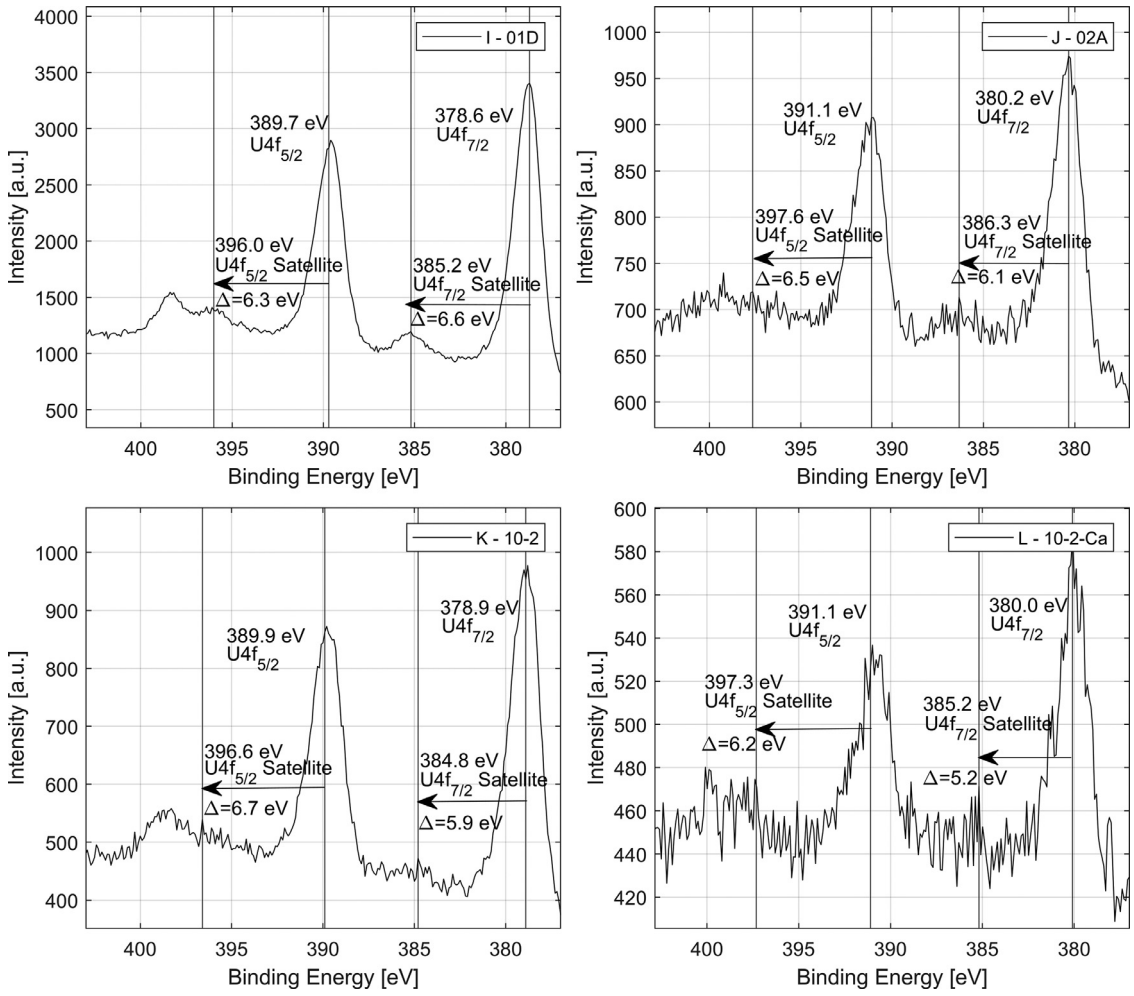

Fig. 10. XPS measurement of the $U4f_{7/2}$ & $U4f_{5/2}$ peaks with the corresponding satellites from experiment batch I-L.

Table 6
Fe(III) to Fe(II) ratios of the Fe2p3/2 peaks of the E-H and I-L experiment batches.

Iron foil label	Fe(III)/Fe(II) ratio
E	0.9753
F	1.2251
G	1.2680
H	0.9619
I	0.9987
J	1.5403
K	1.2868
L	1.3389

Table 2. For experiment batches E-H & I-L the $Fe2p_{3/2}$ deconvolutions are shown in Figs. 12 and 13 respectively.

The corresponding Fe(III)/Fe(II) ratios of the $Fe2p_{3/2}$ peaks are shown in Table 6.

3.4. Speciation calculations

The speciation of uranyl after being added to the synthetic groundwaters under 400 and 3000 ppm CO_2 in Ar atmospheres, before coming in contact with the corroding iron foils, are modelled using PHREEQEC [56], and using the Lawrence Livermore database with the addition of calcium uranyl complexes from the NEA TDB database [26] and the redox assisting element RX together with the Inert elements Ip and Im [57] (Table 7 & Table 8). Under the low partial pressure CO_2 atmosphere, the $Ca_2UO_2(CO_3)_3$ complex dominates in Ca containing groundwaters. As seen from

Table 7
Modelled major uranyl species using PHREEQE C in the 400 ppm CO2 atmosphere experiments.

400 ppm CO_2	01D	02A	10–2	10–2-Ca
$Ca_2UO_2(CO_3)_3$	87.60%	95.39%	0.00%	48.08%
$CaUO_2(CO_3)_3^{2-}$	1.88%	4.28%	0.00%	43.43%
$UO_2(OH)_2$	5.75%	0.00%	3.56%	0.31%
$UO_2(CO_3)_2^{2-}$	2.17%	0.01%	68.09%	5.88%
UO_2CO_3	2.09%	–	1.09%	0.09%
$UO_2(CO_3)_3^{4-}$	–	0.31%	24.51%	2.21%

Table 8
Modelled major uranyl species using PHREEQE C in the 3000 ppm CO_2 atmosphere experiments.

3000 ppm CO_2	01D	02A	10–2	10–2-Ca
$Ca_2UO_2(CO_3)_3$	55.34%	95.39%	–	32.06%
$CaUO_2(CO_3)_3^{2-}$	1.19%	4.27%	–	28.75%
UO_2CO_3	17.06%	–	9.85%	3.90%
$UO_2(OH)_2$	7.18%	0.00%	4.09%	1.64%
$UO_2(CO_3)_2^{2-}$	4.94%	0.02%	78.83%	31.56%
$(UO_2)_2CO_3(OH)_3^-$	1.75%	–	3.43%	0.56%

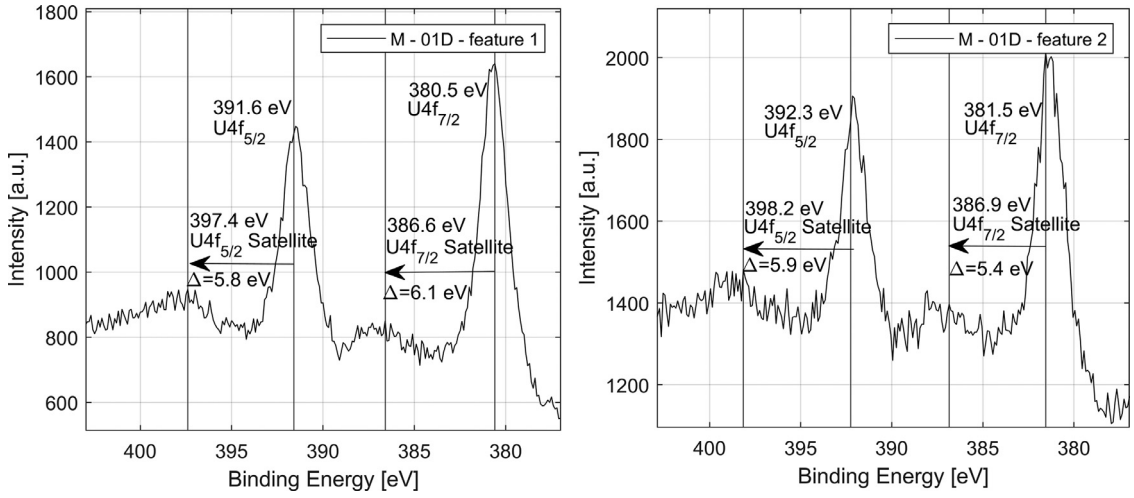

Fig. 11. The $U4f_{7/2}$ and $U4f_{5/2}$ peaks of the crystallite features on the iron foil from experiment M. The energy position in feature 2 represents an oxidized U(VI) state, likely due to the oxygen contamination during the experiment.

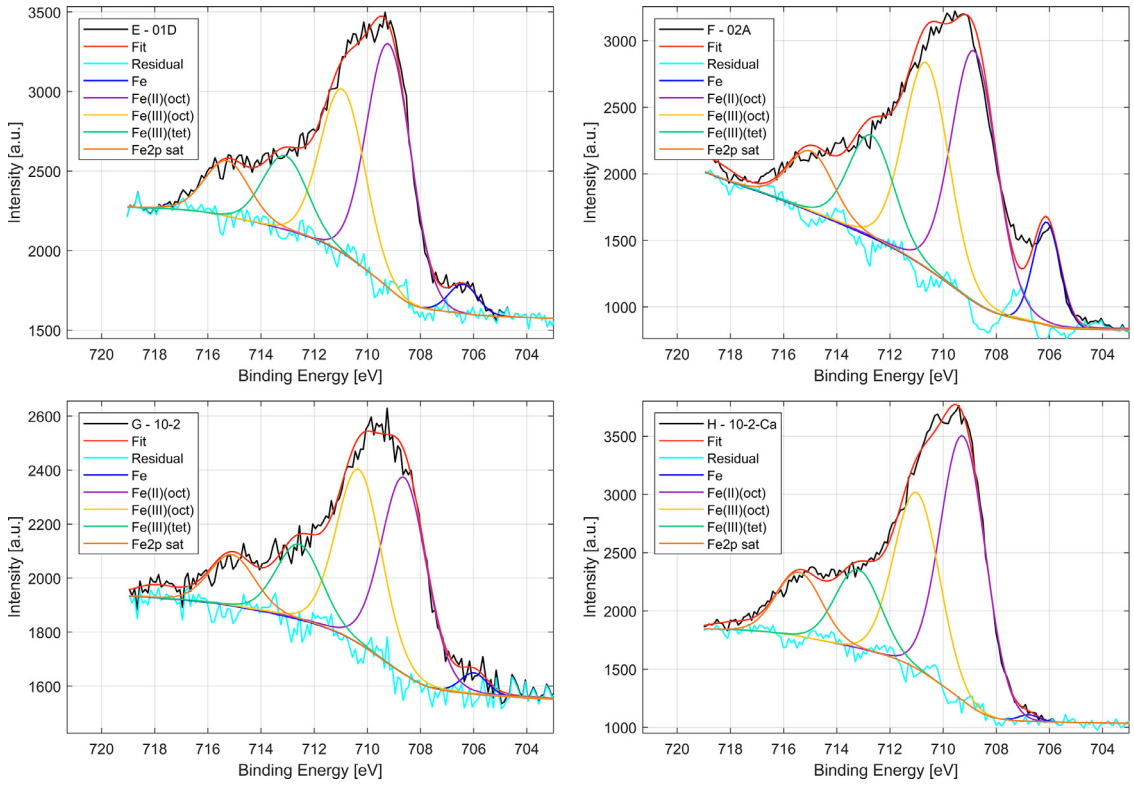

Fig. 12. Deconvolution of the XPS $Fe2p_{3/2}$ peaks of the iron foils from experiments E-H.

the Table 7, calcium-uranyl-carbonato complexes constitute about 90% of the dissolved U in groundwater 01D with 400 ppm CO_2 and 56.5% in the same groundwater with 0.3% CO_2. In synthetic groundwater 02A such complexes dominate much more the uranyl speciation, they constitute ~99.7% of the total U both in 02A with 400 ppm CO_2 and 02A with 3000 ppm CO_2.

3.5. Kinetics of U(VI) reduction

The kinetics of U(VI) removal by corroding metallic iron was investigated by measuring the uranium concentration in solution in experiments A–P at different times (shown in Figs. 2-4, and Fig. 14). Under our experimental conditions, the reductive sites on the iron surface and Fe(II) in solution are much in excess of U(VI). If we plot $\ln(C_t/C_0)$ versus reaction time, where C_t and C_0 are U(VI) concentrations at time t and 0 respectively, we see a nearly linear relationship indicating that the uranium removal closely approximates pseudo-first order reaction kinetics. The natural logarithm of the uranium concentration for the early stages of the experiment, represented by the 5–6 first data points in each test, was fitted by linear least squares and the slope of this line is reported in Table 9 as the pseudo first order rate constant for U(VI) reduction. The higher iron concentrations in experiments A & B did not contribute to faster reduction kinetics, as these higher concentrations were believed not to be due to kinetics, but rather different final equilibrium conditions. With a higher CO_2 pressure, more Fe will be dissolved at equilibrium, which might not affect the kinetics during the initial stages of the experiment.

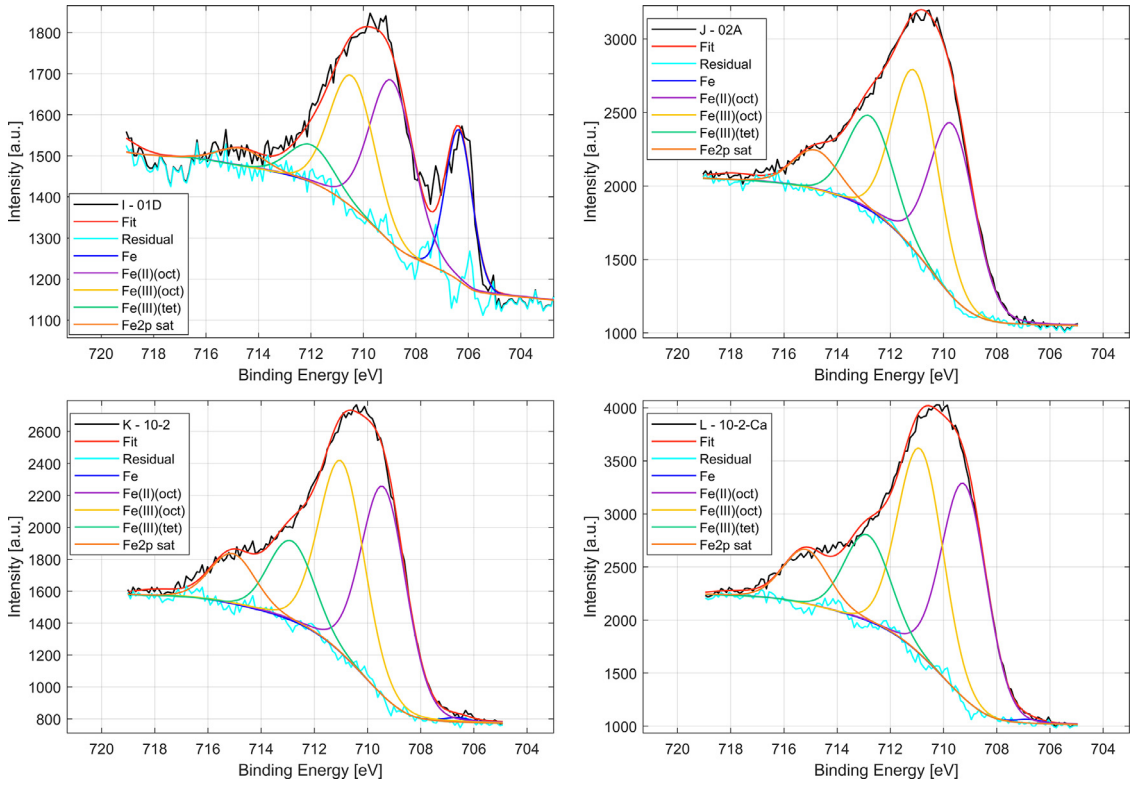

Fig. 13. Deconvolution of the XPS $Fe2p_{3/2}$ of the iron foils from experiments I-L.

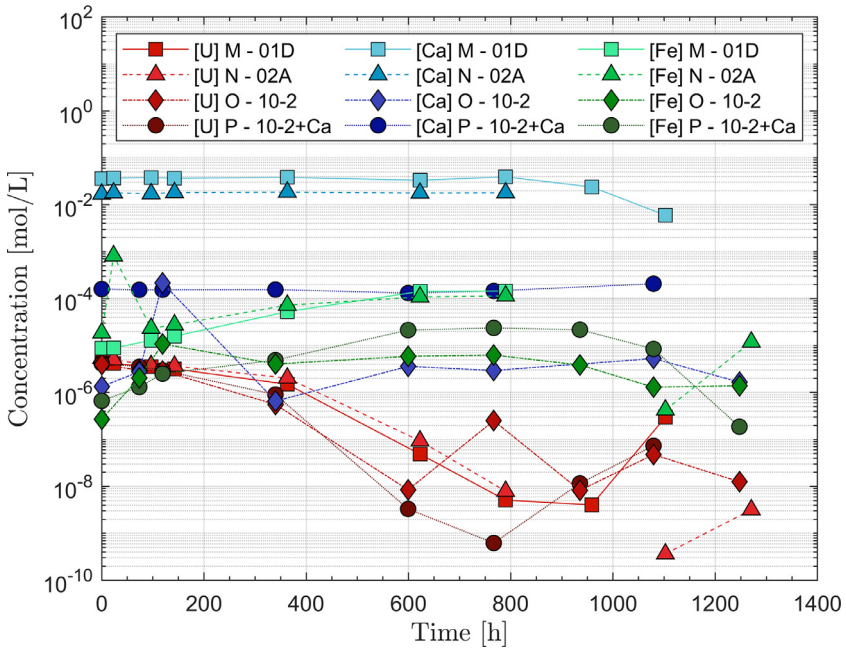

Fig. 14. Dissolved concentrations in the 400 ppm CO_2 Ar atmosphere experiment batch M-P. Air in leakage after 600–800 h led to comparatively high uranium concentrations in solution.

4. Discussion

The rapidly decreasing dissolved uranium concentrations indicate that U(VI) is efficiently reduced and precipitated in solutions containing a corroding iron foil. The higher CO_2 partial pressure (3000 ppm CO_2 in Ar) leads to a higher dissolved CO_2 concentration, increasing the HCO_3^- concentration. The lower uranium concentrations and higher iron concentrations in batch I-L might be due to a higher efficiency of the $FeSO_4$ oxygen trap as compared to the $FeCO_3$ trap, due to the higher Fe(II) concentration in oxygen trap solution, given the higher solubility of $FeSO_4$ [53]. This causes a more efficient removal of the O_2 impurities from the Ar+CO_2 gas mixture as well as more efficiently capture O_2 traces from the glovebox atmosphere.

As can be seen from Table 9, the presence of calcium-uranyl-carbonato complexes decreases the reduction rate of U(VI) some-

Table 9
Pseudo first order rate constants.

Atmosphere	Experiment	Pseudo first order rate constant, d^{-1}
3000 ppm	A - 01D	8.4E-3
CO_2	B - 02A	8.4E-3
	C - 10–2	1.5E-2
	D - 10–2+Ca	1.2E-2
400 ppm	I - 01D	1.4E-2
CO_2	J - 02A	1.8E-2
	K - 10–2	2.2E-2
	L - 10–2+Ca	4.3E-3
400 ppm	M - 01D	5.1E-3
CO_2	N - 02A	3.0E-3
	O - 10–2	5.6E-2
	P - 10–2+Ca	1.5E-2

what in the groundwaters containing calcium as compared to the calcium free 10–2 solution. Thus, at 3000 ppm CO_2, the reduction rate constant is about 1.8 times higher in the 10–2 solution than in the Ca-containing groundwaters, where calcium-uranyl-carbonato complexes constitute more than 99% of uranyl soluble species. The differences are anyhow small. Under our conditions, they appear to be less important than an efficient scavenging of the oxygen traces, which in the case 400 ppm experiments I, J & K causes the highest reduction rates measured, both with and without calcium where again the presence of calcium makes the reduction about 1.2–1.6 times slower (Table 9).

The presence of metallic iron in solution and of the anoxic corrosion products such as magnetite or carbonate green rust on its surface is expected to enhance even reduction caused by Fe(II) sorbed from solution onto their surface [27]. Uranium can also be reduced directly on magnetite [16], or alternatively on carbonate green rust [15,19]. However, the $Fe2p_{3/2}$ peak deconvolution analysis gives a ratio between Fe(III) and Fe(II) fairly close to 1 for all foils in experiment batches E-H and I-L, which represents an oxide with a higher amount of Fe(II) than what is present in magnetite. At the same time, this ratio is lower than the amount of Fe(II) expected from most green rust compositions [54], which could indicate a mixture of the two different oxides. Uranium was observed to be precipitated on top of carbonate rich spots on the iron foil surfaces, likely in conjunction with the carbonate green rust corrosion product. This corresponds well with the results from the work of Cui and Spahiu, where uranium was precipitated on top of green rust under analogous experimental conditions [15], and the results from O'Loughlin, which showed that UO_2 nanoparticles were formed by the reductive action of green rust [19].

Comparing the last data points in experiments I & K to those of J & L, the corresponding uranium concentrations of the former are lower by approximately an order of magnitude compared to the latter (Fig. 4). The significantly higher amount of U precipitation can also be observed from both the relative intensities in the XPS measurement (Fig. 10) as well as from the larger grain size in experiment K compared to L as shown in Fig. 8.

The $U4f_{7/2}$ peaks in experiments E-H have energies very similar to that of U(IV) at 380.0 ± 0.2 eV shown in Table 1, indicating that the uranium on the iron foils is in the reduced U(IV) state. As seen in a previous work by our group where UO_2-pellets were measured, the $U4f_{7/2}$ peak position was shifted to an energy of ~379.5 eV due to the charging correction procedure [37]. This same shift is likely not present in the measurement of precipitated uranium on the iron foils as the $U4f_{7/2}$ peak energy is close to 380 eV, with corresponding satellites which are quite well aligned with the U(IV) satellite shift energy of 6.9 ± 0.5 eV. The satellite shift is however on the lower end or even below of expected range for several peaks. Nevertheless, this is not indicative of U(V), as the satellites would have an increase in the binding energy position (Table 1).

5. Conclusion

The understanding of UO_2 migration behavior in groundwater solution in the presence of iron is important in the safety assessment of a geological final repository as well as for predicting the behavior of dissolved uranium in the environment. The work experimentally shows that there is an additional reducing capacity in the system from metallic iron in the fuel canister inserts. This was shown through the strong reducing effect by the iron foils, reducing the initially present ~$4.2 \cdot 10^{-6}$ M uranium to approximately three orders of magnitude lower concentrations in all groundwater compositions in the long term, quite like those in equilibrium with UO_2(am) [22].

The investigation of iron foil surfaces after test conclusion with SEM-EDS and XPS confirmed uranium precipitation as UO_2(s) on top of the iron foil surfaces as radially growing particles, producing particles with relatively large radii considering the low total uranium amounts in solution. This precipitation likely occurred on carbonate green rust formed on corroding iron surface, observed as dark green spots (see Fig. 5a and b).

The presence of calcium-uranyl-carbonato species did not inhibit the reductive precipitation in contact with a corroding metallic iron surface, even though the reduction was slightly slower in the presence of Ca. In a repository canister breach scenario, potentially dissolved UO_2 in the U(VI) oxidation state would then be expected to be reduced and probably re-deposited as UO_2 particles on the corroding iron surface of the canister insert.

Declaration of competing interest

The authors declare that they have no known competing financial interests or personal relationships that could have appeared to influence the work reported in this paper.

The authors declare the following financial interests/personal relationships which may be considered as potential competing interests:

Niklas L. Hansson reports financial support was provided by Swedish Nuclear Fuel and Waste Management Co. Niklas L. Hansson reports a relationship with Swedish Nuclear Fuel and Waste Management Co that includes: funding grants.

CRediT authorship contribution statement

N.L. Hansson: Conceptualization, Formal analysis, Investigation, Methodology, Visualization, Writing – original draft, Writing – review & editing. **M. Saleh:** Investigation, Writing – review & editing. **P.L. Tam:** Investigation, Formal analysis, Writing – review & editing. **S. Holgersson:** Investigation, Writing – review & editing. **K. Spahiu:** Conceptualization, Supervision, Writing – review & editing. **C. Ekberg:** Conceptualization, Supervision, Methodology, Writing – review & editing.

Data availability

Data will be made available on request.

Acknowledgements

Swedish Nuclear and Fuel and Waste Management Co. are greatly acknowledged for funding of this research. We thank Dr. Daqing Cui for help with the experimental setup and Dr. Ignasi Puigdomenech for help with the choice of representative compositions of Forsmark groundwaters.

Appendix

In the batch with experiments M-P, the partial pressure of O_2 reached a level of ~80 ppm around 600–800 h, due to the glove-box Ar gas supply running empty for a brief time period. This led to uranium concentrations fluctuating quite significantly in the 10^{-9}–10^{-7} M range during the remainder of the experiment. The resulting iron concentrations were lower than those found in experiment batch A-D & I-L.

References

[1] F. King, L. Ahonen, C. Taxén, U. Vuorinen, L. Werme, Copper Corrosion Under Expected Conditions in a Deep Geologic Repository, Swedish Nuclear Fuel and Waste Management Co, 2001.

[2] I. Puigdomenech, J. Ambrosi, L. Eisenlohr, J. Lartigue, S. Banwart, K. Bateman, A. Milodowski, J. West, L. Griffault, E. Gustafsson, O2 Depletion in Granitic Media. The Rex Project, Swedish Nuclear Fuel and Waste Management Co, 2001.

[3] N. Giroud, Y. Tomonaga, P. Wersin, S. Briggs, F. King, T. Vogt, N. Diomidis, On the fate of oxygen in a spent fuel emplacement drift in Opalinus Clay, Appl. Geochem. 97 (2018) 270–278.

[4] M. Badley, D. Shoesmith, The Corrosion/Dissolution of Used Nuclear Fuel in a Deep Geological Repository, Nuclear Waste Management Organization, Toronto, Canada, 2022 Technical Report NWMO-TR-2022-09.

[5] Svensk Kärnbränslehantering A.B., Technical Report TR-11-01 - Long-term safety for the final repository for spent nuclear fuel at Forsmark. Main report of the SR-Site project., (2011).

[6] B. Bonin, M. Colin, A. Dutfoy, Pressure building during the early stages of gas production in a radioactive waste repository, J. Nucl. Mater. 281 (2000) 1–14.

[7] E. Ekeroth, M. Granfors, D. Schild, K. Spahiu, The effect of temperature and fuel surface area on spent nuclear fuel dissolution kinetics under H2 atmosphere, J. Nucl. Mater. 531 (2020) 151981, doi:10.1016/j.jnucmat.2019.151981.

[8] A. Puranen, A. Barreiro, L.-.Z. Evins, K. Spahiu, Spent fuel corrosion and the impact of iron corrosion–the effects of hydrogen generation and formation of iron corrosion products, J. Nucl. Mater. 542 (2020) 152423, doi:10.1016/j.jnucmat.2020.152423.

[9] M. Odorowski, C. Jegou, L. De Windt, V. Broudic, G. Jouan, S. Peuget, C. Martin, Effect of metallic iron on the oxidative dissolution of UO2 doped with a radioactive alpha emitter in synthetic Callovian-Oxfordian groundwater, Geochimica et Cosmochimica Acta 219 (2017) 1–21.

[10] J. Farrell, W.D. Bostick, R.J. Jarabek, J.N. Fiedor, Uranium removal from ground water using zero valent iron media, Groundwater 37 (1999) 618–624, doi:10.1111/j.1745-6584.1999.tb01150.x.

[11] J.N. Fiedor, W.D. Bostick, R.J. Jarabek, J. Farrell, Understanding the mechanism of uranium removal from groundwater by zero-valent iron using X-ray photoelectron spectroscopy, Environ. Sci. Technol. 32 (1998) 1466–1473, doi:10.1021/es970385u.

[12] B. Gu, L. Liang, M. Dickey, X. Yin, S. Dai, Reductive precipitation of uranium (VI) by zero-valent iron, Environ. Sci. Technol. 32 (1998) 3366–3373, doi:10.1021/es980010o.

[13] S.J. Morrison, D.R. Metzler, C.E. Carpenter, Uranium precipitation in a permeable reactive barrier by progressive irreversible dissolution of zerovalent iron, Environ. Sci. Technol. 35 (2001) 385–390, doi:10.1021/es001204i.

[14] B. Grambow, E. Smailos, H. Geckeis, R. Müller, H. Hentschel, Sorption and reduction of uranium (VI) on iron corrosion products under reducing saline conditions, Radiochimica Acta 74 (1996) 149–154, doi:10.1524/ract.1996.74.special-issue.149.

[15] D. Cui, K. Spahiu, The reduction of U (VI) on corroded iron under anoxic conditions, Radiochimica Acta 90 (2002) 623–628.

[16] Z. Pan, B. Bártová, T. LaGrange, S.M. Butorin, N.C. Hyatt, M.C. Stennett, K.O. Kvashnina, R. Bernier-Latmani, Nanoscale mechanism of UO2 formation through uranium reduction by magnetite, Nature Commun. 11 (2020) 1–12, doi:10.1038/s41467-020-17795-0.

[17] D.E. Latta, B. Mishra, R.E. Cook, K.M. Kemner, M.I. Boyanov, Stable U (IV) complexes form at high-affinity mineral surface sites, Environ. Sci. Technol. 48 (2014) 1683–1691, doi:10.1021/es4047389.

[18] T. Scott, G. Allen, P. Heard, M. Randell, Reduction of U (VI) to U (IV) on the surface of magnetite, Geochim. Cosmochim. Acta 69 (2005) 5639–5646, doi:10.1016/j.gca.2005.07.003.

[19] E.J. O'Loughlin, S.D. Kelly, R.E. Cook, R. Csencsits, K.M. Kemner, Reduction of uranium (VI) by mixed iron (II)/iron (III) hydroxide (green rust): formation of UO2 nanoparticles, Environ. Sci. Technol. 37 (2003) 721–727, doi:10.1021/es0208409.

[20] E. Liger, L. Charlet, P. Van Cappellen, Surface catalysis of uranium (VI) reduction by iron (II), Geochim. Cosmochim. Acta 63 (1999) 2939–2955, doi:10.1016/S0016-7037(99)00265-3.

[21] X. Du, B. Boonchayaanant, W.-.M. Wu, S. Fendorf, J. Bargar, C.S. Criddle, Reduction of uranium (VI) by soluble iron (II) conforms with thermodynamic predictions, Environ. Sci. Technol. 45 (2011) 4718–4725, doi:10.1021/es2006012.

[22] R. Guillamont, T. Fanghanel, I. Grenthe, V. Neck, D. Palmer, M. Rand, Update on the chemical thermodynamics of uranium, neptunium, plutonium, americium and technetium, Nuclear Energy Agency Data Bank, Organization for Economic Co-operation, Development 5 (2003).

[23] G. Bernhard, G. Geipel, V. Brendler, H. Nitsche, Speciation of uranium in seepage waters of a mine tailing pile studied by time-resolved laser-induced fluorescence spectroscopy (TRLFS), Radiochimica Acta 74 (1996) 87–92.

[24] G. Bernhard, G. Geipel, T. Reich, V. Brendler, S. Amayri, H. Nitsche, Uranyl (VI) carbonate complex formation: validation of the Ca2UO2 (CO3) 3 (aq.) species, Radiochimica Acta 89 (2001) 511–518.

[25] F. Endrizzi, L. Rao, Chemical speciation of uranium (VI) in marine environments: complexation of calcium and magnesium Ions with [(UO2)(CO3) 3] 4− and the effect on the extraction of uranium from seawater, Chem.–Eur. J. 20 (2014) 14499–14506.

[26] I. Grenthe, X. Gaona, Second Update on the Chemical Thermodynamics of Uranium, Neptunium, plutonium, Americium and Technetium, OECD/NEA Publishing, 2020.

[27] C. Dewey, D. Sokaras, T. Kroll, J.R. Bargar, S. Fendorf, Calcium-uranyl-carbonato species kinetically limit U (VI) reduction by Fe (II) and lead to U (V)-bearing ferrihydrite, Environ. Sci. Technol. 54 (2020) 6021–6030, doi:10.1021/acs.est.9b05870.

[28] S.C. Brooks, J.K. Fredrickson, S.L. Carroll, D.W. Kennedy, J.M. Zachara, A.E. Plymale, S.D. Kelly, K.M. Kemner, S. Fendorf, Inhibition of bacterial U (VI) reduction by calcium, Environ. Sci. Technol. 37 (2003) 1850–1858, doi:10.1021/es0210042.

[29] K.M. Belli, T.J. DiChristina, P. Van Cappellen, M. Taillefert, Effects of aqueous uranyl speciation on the kinetics of microbial uranium reduction, Geochim. Cosmochim. Acta 157 (2015) 109–124, doi:10.1016/j.gca.2015.02.006.

[30] P.M. Fox, J.A. Davis, J.M. Zachara, The effect of calcium on aqueous uranium (VI) speciation and adsorption to ferrihydrite and quartz, Geochim. Cosmochim. Acta 70 (2006) 1379–1387, doi:10.1016/j.gca.2005.11.027.

[31] B.D. Stewart, M.A. Mayes, S. Fendorf, Impact of uranyl− calcium− carbonato complexes on uranium (VI) adsorption to synthetic and natural sediments, Environ. Sci. Technol. 44 (2010) 928–934.

[32] L. Agrenius, K. Spahiu, Criticality Effects of Long-Term Changes in Material Compositions and Geometry in Disposal Canisters, SKB, 2016 TR-16-06.

[33] N. Yamada, Kinetic energy discrimination in collision/reaction cell ICP-MS: theoretical review of principles and limitations, Spectrochimica Acta Part B: Atomic Spectrosc. 110 (2015) 31–44, doi:10.1016/j.sab.2015.05.008.

[34] T.M. Willey, A.L. Vance, T. Van Buuren, C. Bostedt, L. Terminello, C. Fadley, Rapid degradation of alkanethiol-based self-assembled monolayers on gold in ambient laboratory conditions, Surf. Sci. 576 (2005) 188–196.

[35] M. Seah, Summary of ISO/TC 201 Standard: VII ISO 15472: 2001—Surface chemical analysis—X-ray photoelectron spectrometers—calibration of energy scales, Surf. Interface Anal. 31 (2001) 721–723.

[36] G. Greczynski, L. Hultman, A step-by-step guide to perform x-ray photoelectron spectroscopy, J. Appl. Phys. 132 (2022) 011101.

[37] N. Hansson, P. Tam, C. Ekberg, K. Spahiu, XPS study of external α-radiolytic oxidation of UO2 in the presence of argon or hydrogen, J. Nucl. Mater. 543 (2021) 152604, doi:10.1016/j.jnucmat.2020.152604.

[38] S. Van den Berghe, J.-.P. Laval, B. Gaudreau, H. Terryn, M. Verwerft, XPS investigations on cesium uranates: mixed valency behaviour of uranium, J. Nucl. Mater. 277 (2000) 28–36.

[39] T. Yamashita, P. Hayes, Analysis of XPS spectra of Fe2+ and Fe3+ ions in oxide materials, Appl. Surf. Sci. 254 (2008) 2441–2449, doi:10.1016/j.apsusc.2007.09.063.

[40] M. Mullet, V. Khare, C. Ruby, XPS study of Fe(II)-Fe(III) (oxy)hydroxycarbonate green rust compounds, Surf. Interface Ana. 40 (2008) 323–328, doi:10.1002/sia.2758.

[41] T.-.C. Lin, G. Seshadri, J.A. Kelber, A consistent method for quantitative XPS peak analysis of thin oxide films on clean polycrystalline iron surfaces, Appl. Surf. Sci. 119 (1997) 83–92, doi:10.1016/S0169-4332(97)00167-0.

[42] E.S. Ilton, P.S. Bagus, XPS determination of uranium oxidation states, Surf. Interface Anal. 43 (2011) 1549–1560.

[43] K.I. Maslakov, Y.A. Teterin, S.V. Stefanovsky, S.N. Kalmykov, A.Y. Teterin, K.E. Ivanov, XPS study of uranium-containing sodium-aluminum-iron-phosphate glasses, J. Alloys Compounds 712 (2017) 36–43.

[44] T. Gouder, R. Eloirdi, R. Caciuffo, Direct observation of pure pentavalent uranium in U 2 O 5 thin films by high resolution photoemission spectroscopy, Sci. Rep. 8 (2018) 1–7.

[45] B. Santos, H. Nesbitt, J. Noel, D. Shoesmith, X-ray photoelectron spectroscopy study of anodically oxidized SIMFUEL surfaces, Electrochimica Acta 49 (2004) 1863–1873.

[46] A. Grosvenor, B. Kobe, M. Biesinger, N. McIntyre, Investigation of multiplet splitting of Fe 2p XPS spectra and bonding in iron compounds, Surf. Interface Anal. 36 (2004) 1564–1574, doi:10.1002/sia.1984.

[47] C. Yang, G. Wang, Z. Lu, J. Sun, J. Zhuang, W. Yang, Effect of ultrasonic treatment on dispersibility of Fe3O4 nanoparticles and synthesis of multi-core Fe3O4/SiO2 core/shell nanoparticles, J. Mater. Chem. 15 (2005) 4252–4257, doi:10.1039/B505018A.

[48] R. Crane, T. Scott, The effect of vacuum annealing of magnetite and zero-valent Iron nanoparticles on the removal of aqueous uranium, J. Nanotechnol. (2013) 2013, doi:10.1155/2013/173625.

[49] F.M. Piras, A. Rossi, N.D. Spencer, Combined in situ (ATR FT-IR) and ex situ (XPS) study of the ZnDTP-iron surface interaction, Tribol. Lett. 15 (2003) 181–191, doi:10.1023/A:1024800900716.

[50] N. Eglizaud, F. Miserque, E. Simoni, M. Schlegel, M. Descostes, Uranium (VI) interaction with pyrite (FeS2): chemical and spectroscopic studies, Radiochimica Acta 94 (2006) 651–656, doi:10.1524/ract.2006.94.9-11.651.

[51] M. Laaksoharju, J. Smellie, E.-L. Tullborg, M. Gimeno, L. Hallbeck, J. Molinero, N. Waber, Bedrock hydrogeochemistry Forsmark, Site Descriptive Modelling SDM-Site Forsmark, 2008.
[52] M.Y. Nassar, I.S. Ahmed, T.Y. Mohamed, M. Khatab, A controlled, template-free, and hydrothermal synthesis route to sphere-like α-Fe 2 O 3 nanostructures for textile dye removal, Rsc Adv. 6 (2016) 20001–20013, doi:10.1039/C5RA26112K.
[53] P. Bénézeth, J. Dandurand, J. Harrichoury, Solubility product of siderite (FeCO3) as a function of temperature (25–250 C), Chem. Geol. 265 (2009) 3–12.
[54] L.H. Chaves, The role of green rust in the environment: a review, Revista Brasileira de Engenharia Agrícola e Ambiental 9 (2005) 284–288, doi:10.1590/S1415-43662005000200021.
[55] R. Taylor, R. McKenzie, The influence of aluminum on iron oxides. VI. The formation of Fe (II)-Al (III) hydroxy-chlorides,-sulfates, and-carbonates as new members of the pyroaurite group and their significance in soils, Clays Clay Miner 28 (1980) 179–187, doi:10.1346/CCMN.1980.0280303.
[56] D.L. Parkhurst, C. Appelo, Description of input and examples for PHREEQC version 3—a computer program for speciation, batch-reaction, one-dimensional transport, and inverse geochemical calculations, US Geol. Surv. Tech. Methods 6 (2013) 497.
[57] C. Ekberg, A. Emrén, Finding and correcting calculation errors in PHREEQE, 4th Int. Conf. on the Chem. and Migr. Behaviour of Actinides and Fission Products in the Geosphere, Charleston, SC USA, Dec. 12-17, 1993, Oldenbourg Verlag, Munich, 1994.